Iterative Methods for Waveform Control in Magnetic Measurement Systems

Patrick Fagan, Benjamin Ducharne, Stanislaw Zurek, *Senior Member, IEEE*, Mathieu Domenjoud, Anastasios Skarlatos, *Member, IEEE*, Laurent Daniel, and Christophe Reboud

***Abstract*— Magnetic losses in a ferromagnetic lamination can be separated into three contributions. Bertotti theoretically assessed this distribution at the end of the twentieth century in the statistical theory of losses (STLs), triggering significant progress in understanding the dissipation mechanisms. Recent studies have shown the possibility of reconstructing a hysteresis cycle from the high-frequency Barkhausen noise signal. Applying STL to the Barkhausen noise cycles has never been done before. Still, it could help establish a parallel with the measurement of the magnetization cycle versus frequency and the energy loss. However, STL analysis in its ultimate description requires sinusoidal flux density, while Barkhausen noise measurements are usually done with a constant excitation slope. Multiple magnetic flux density control methods were described in the literature and are reviewed in this article. However, the Barkhausen noise context, requiring high-frequency sampling during the magnetization cycle, is more constraining. Therefore, specific performance criteria were considered, followed by numerical tests to determine the most adapted method to a Barkhausen STL description. Eventually, the proportional iterative learning control (P-ILC) gave the highest satisfaction rate and was chosen for experimental tests. Some of these experimental results are provided in this article discussion together with suggestions for convergence speed improvement. It is, for instance, recommended to increase the gain near saturation, where the system response is poor.**

***Index Terms*— Feedback, flux density, magnetic Barkhausen noise energy, magnetic losses, waveform control.**

I. Introduction

MAGNETIC cores are omnipresent in electrical energy conversion and transport. Losses inevitably happen while magnetic cores operate and are a significant cause of inefficiency. During one magnetization cycle, these losses are equivalent to the area of the $B_a(H_{\text{surf}})$ hysteresis cycle obtained by plotting the flux density B_a averaged through the tested specimen cross section as a function of the tangent surface excitation field H_{surf} [1]

$$P = \oint B_a(H_{\text{surf}}) \cdot \mathrm{d}H_{\text{surf}}. \tag{1}$$

The first attempts for the hysteresis losses prediction trace back to Steinmetz's model [(2)] [2], [3]. This empirical relation was limited to sinusoidal B_a conditions and stated that iron losses followed a fractional power "law" of both frequency f and $B_{a_{\max}}$ (peak value of sinusoidal B_a)

$$P = k \cdot f^a \cdot B_{a_{\max}}^b \tag{2}$$

where k, a, and b are the three constant parameters depending on the nature and geometry of the magnetic circuit. Loss separation was initially proposed in 1924 with Jordan's work [4], who assumed that magnetic core losses could be divided [(3)] into a static contribution P_{st} and a dynamic contribution related to classical eddy current loss P_{cl} [4], [5], [6]

$$P = P_{\text{st}} + P_{\text{cl}} = \alpha \cdot f + \beta \cdot f^2 \tag{3}$$

where α and β are the fit parameters. This simple approach was later improved by adding an excess loss term to match the experimental data, wrongly approximated by (3) (grain-oriented electrical steels FeSi GO [7]). Initially, the physical justification for the additional contribution was unknown, and it was even referred to as "anomalous" loss. It was obtained by either modifying β or simply adding a third contribution or "excess" loss (P_{exc}) [8]

$$P = P_{\text{st}} + P_{\text{cl}} + P_{\text{exc}}. \tag{4}$$

This empirical method found theoretical foundations from Bertotti's Statistical Theory of Losses (STLs) [9], expressed in terms of power in (5) or energy in (6) (a_{st}, a_{cl}, and a_{exc} are the fitting parameters)

$$P = a_{\text{st}} f + a_{\text{cl}} f^2 + a_{\text{exc}} f^{\frac{3}{2}} \tag{5}$$

$$W(f) = \frac{P}{f} = a_{\text{st}} + a_{\text{cl}} f + a_{\text{exc}} \sqrt{f}. \tag{6}$$

STL is an advanced theoretical method that brought significant progress in understanding the magnetization mechanisms [10], [11], [12], [13], [14], [15], [16]. It is, however, worth mentioning that supposes a full flux penetration which restricts its domain of validity to approximately 100 Hz for a typical FeSi GO (thickness = 300 μm).

Manuscript received 6 April 2022; revised 23 July 2022; accepted 27 July 2022. Date of publication 2 September 2022; date of current version 12 September 2022. The Associate Editor coordinating the review process was Libing Bai. *(Corresponding author: Benjamin Ducharne.)*

Patrick Fagan, Anastasios Skarlatos, and Christophe Reboud are with LIST, CEA, CNRS, CEA Saclay, Université Paris-Saclay, 91191 Gif-sur-Yvette, France.

Benjamin Ducharne is with ELyTMaX IRL3757, CNRS, Université de Lyon, INSA Lyon, Centrale Lyon, Université Claude Bernard Lyon 1, Tohoku University, Sendai 980-8577, Japan, and also with the Laboratoire de Génie Electrique et Ferroélectricité (LGEF), INSA Lyon, 69100 Villeurbanne, France (e-mail: benjamin.ducharne@insa-lyon.fr).

Stanislaw Zurek is with Megger Instruments, Dover CT17 9EN, U.K.

Mathieu Domenjoud and Laurent Daniel are with Université Paris-Saclay, CentraleSupélec, CNRS, Laboratoire de Génie Electrique et Electronique de Paris, 91192 Gif-sur-Yvette, France, and also with Sorbonne Université, CNRS, Laboratoire de Génie Electrique et Electronique de Paris, 75252 Paris, France.

Digital Object Identifier 10.1109/TIM.2022.3199198

Recent works [17], [18], [19] have demonstrated the feasibility of plotting hysteresis cycles from Barkhausen noise measurement. For this, the so-called magnetic Barkhausen noise energy $\mathrm{MBN}_{\mathrm{energy}}$ [(7)] is plotted as a function of H_{surf}

$$\mathrm{MBN}_{\mathrm{energy}}(t) = \nu \cdot \int_0^{\mathrm{t}} \mathrm{sign}\left(\frac{\mathrm{dH}_{\mathrm{surf}}}{\mathrm{ds}}\right) \cdot V_{\mathrm{MBN}}^2(s) \cdot ds \tag{7}$$

where ν is a normalization coefficient and V_{MBN} is the magnetic Barkhausen noise voltage drop across the sensor coil. Compared with the classic $B_a(H_{\mathrm{surf}})$, $\mathrm{MBN}_{\mathrm{energy}}(H_{\mathrm{surf}})$ hysteresis cycles depend on the excitation frequency and, thus, reflect physical properties. It is, therefore, tempting to apply STL to these alternative cycles and get additional insights regarding the physics of the magnetization mechanisms. $\mathrm{MBN}_{\mathrm{energy}}$ is linked predominantly to the magnetic domain wall motions; thus, in the $\mathrm{MBN}_{\mathrm{energy}}$ STL, the classical loss contribution, related to the macroscopic eddy currents and first-order-frequency-dependent, should be negligible. Hence, the frequency dependency of the $\mathrm{MBN}_{\mathrm{energy}}$ hysteresis cycle energy is expected to be written as in the following equation:

$$W_{\mathrm{MBN}_{\mathrm{energy}}}(f) = b_{\mathrm{st}} + b_{\mathrm{exc}} \cdot \sqrt{f} \tag{8}$$

with b_{st} and b_{exc} are the two constants. Equation (8) is purely hypothetical and has never been validated by comparison to experimental results. By increasing the magnetization frequency, the available frequency band of the MBN spectral density is expected to shift upward. Still, this effect remains unclear and the comparison with STL is expected to bring clarification. Even if STL was originally developed, for the sake of simplicity, by assuming that the magnetization process occurs under controlled macroscopic constant induction derivative (triangular induction), the ensuing formulation was successively modified to comply with sinusoidal and generic induction waveform. Equation (6) supposes this condition to be respected [15]. In the case of Barkhausen noise measurements, either the excitation current or the magnetic excitation H_{surf} is usually imposed triangular [21], [22] and measurements are rarely done under sinusoidal flux density. $B_a(H_{\mathrm{surf}})$ and $\mathrm{MBN}_{\mathrm{energy}}(H_{\mathrm{surf}})$ can be obtained from the same experimental setup. Therefore, a suitable method for the flux density control during Barkhausen noise measurement can be inspired by published work related to standard hysteresis characterizations [23], [24], [25], [26], [27], [28], [29], [30]. Still, additional constraints owed to Barkhausen noise measurement have to be considered before setting the most adapted method. A magnetic characterization setup contains two nonlinear elements. (The inductor yoke used to drive the magnetic field H_{surf} and the tested sample.) Analytical solutions are sometimes proposed for setting the induction control system. Still, the effect of hysteresis and the to-be-measured properties of the specimen make them approximative; hence, iterative methods prevail. The focus of this article is to examine a wide range of digital feedback methods found in the literature to assure a sinusoidal flux density during hysteresis measurements and select the most appropriate one for the specific context of the Barkhausen noise STL application. Comparisons exist in [31], but they are limited to two or three methods and never deal with the specific Barkhausen noise perspective. The study is restricted to digital feedback methods [24], [25], [26], [27], [28], [29], [30]. Even if widespread before the proliferation of computers, the analog feedback methods [30], [32], [33] are poorly tunable and less robust since they rely on discrete components whose values can be challenging to set, especially if heated. Analog systems work in real time. Perturbations cannot be anticipated, and high precisions cannot be reached on a wide range of frequencies and materials. Other problems can arise if the system is strongly nonlinear and has unstable feedback [20]. It should also be noted that high-gain high-bandwidth analog (real time) feedback can suppress large-amplitude Barkhausen noise activity [1], [20]. For the same reasons, this article will not consider hybrid methods (obtained by combining digital and analog feedback methods [34], [35]).

II. Review of Iterative Feedback Methods

A. Performance Criteria

This study aims to define and test the most efficient magnetic flux density control method in the context of the $\mathrm{MBN}_{\mathrm{energy}}$ hysteresis cycle characterization and STL application [21], [22], [36]. To obtain adapted comparisons and reach our objective, a specific series of criteria has been defined as follows.

1) *Number of Iterations*: a reduced number of iterations is important, especially in the low-frequency range where a measure can take several minutes and generate large data files complex to process. It is also critical in the high-frequency range, where thermal transfers due to the magnetic losses can affect the experimental conditions and the magnetic response of the material.
2) *Accuracy*: Convergence should be reached with a minimum error. Error estimations can take different forms, including relative Euclidean difference, form factor difference, Pearson dissimilarity, and total harmonic distortion.
3) *Number of Parameters*: Feedback control parameters must be tuned for each new experimental situation. Optimizing a large number of parameters requires a lot of experimental data.
4) *Robustness*: The feedback method should remain undisturbed by external stimuli, including white noises, drifts, and offsets.
5) *Memory Allocation and Computation Time Efficiency*: The ideal feedback method computes an iteration with reduced time and limited memory capacity. This criterion is especially detrimental to techniques based on square matrix inversion requiring high computation capacity and large memory allocation.
6) *Universality*: This criterion is related to the capability of providing satisfactory results in different experimental conditions without extensive calibrations processes.

A feedback method providing a positive answer to all the criteria listed above does not exist. Many approaches have been described in [21], [22], [23], [24], [25], [26], and [27], and each technique can perform well in specific conditions. This study aims to compare these methods to find the most

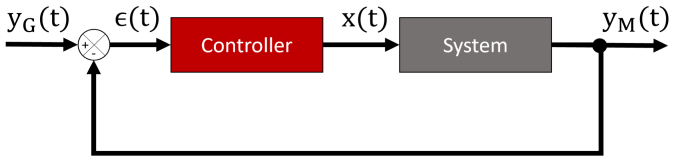

Fig. 1. Feedback structure.

suitable feedback technique in the particular context of the $\mathrm{MBN}_{\mathrm{energy}}(H_{\mathrm{surf}})$ hysteresis cycles characterization.

B. Detailed Description of Iterative Feedback Methods

Let us introduce the feedback notation and a general feedback scheme (Fig. 1).

1) $Y_G(t)$ is the reference, i.e., the ideal desired goal output (at time t).
2) $y_M(t, j)$ is the measured output of iteration j (at time t).
3) $\epsilon(\mathrm{t}, \mathrm{j}) = y_G(t) - y_M(t, j)$ is the error of jth iteration (at time t).
4) $\mathrm{x}(t, j)$ is the system input of jth iteration (at time t).

1) Iterative Learning Control: A straightforward iterative method for the control of a nonlinear system can be derived from the classical real-time proportional integral derivative (PID) technique

$$x(t) = K_P \cdot \epsilon(t) + K_I \cdot \int_0^t \epsilon(s)\mathrm{d}s + K_D \cdot \frac{\mathrm{d}\epsilon}{\mathrm{d}t} \tag{9}$$

with K_p, K_I, and K_D are the proportional, integral, and derivative gains, respectively. The iterative PID method has been described by several authors, including Gruebler *et al.* [37], and consists in

$$x(t, j+1) = x(t, j) + \Delta x(t, j) \tag{10}$$

$$\Delta x(t, j) = K_P \cdot \epsilon(t, j) + K_I \cdot \int_0^t \epsilon(s, j)\mathrm{d}s + K_D \cdot \frac{\mathrm{d}\epsilon}{\mathrm{d}t}(t, j). \tag{11}$$

In their simplest form (proportional correction only), the above equations can be simplified, which leads to the proportional-iterative learning control formulation (P-ILC) [37]

$$x(t, j+1) = x(t, j) + K_P \cdot \epsilon(t, j). \tag{12}$$

The phase-lead iterative learning control (ILC) method is similar to P-ILC but involves the addition of a constant delay τ in the error term [38], [39]

$$x(t, j+1) = x(t, j) + K_P \cdot \epsilon(t+\tau, j). \tag{13}$$

P-ILC is simple; the inputs are reduced to $\epsilon(t, j)$, and parameters to K_p. Its implementation is very straightforward, and, like classic PID, it can be very robust with the right choice of K_p. However, the choice between high gain/fast convergence and small gain/no divergence makes the optimization tricky, typically ending with a slower convergence speed at the benefit of better robustness.

2) Fourier Series Proportional-Iterative Learning Control: Switching from the time domain to the frequency domain can be highly beneficial by simplifying mathematical operations. The Fourier transform being linear, the following equations become (15):

$$x(t, j+1) = x(t, j) + K_P \cdot [y_G(t) - y_M(t, j)] \tag{14}$$

$$X(f, j+1) = X(f, j) + K_P \cdot [Y_G(f) - Y_M(f, j)] \tag{15}$$

where $X(f, j)$ is the Fourier transform of $x(t, j)$. Fourier transforms lead to complex numbers, and Fourier series proportional-iterative learning control (FSP-ILC) works with complex number formalism. While Fourier distribution iterative learning control (FDP-ILC) would apply (15) to the whole frequency spectrum, FSP-ILC is limited only to the excitation frequency's multiples (f_{exc}) and can even be reduced to those of substantial contribution. The following equation gives FSP-ILC equation when $k \in [1\ -M]$

$$X(k \cdot f_{\mathrm{exc}}, j+1) = X(k \cdot f_{\mathrm{exc}}, j) + K_P \cdot [Y_G(k \cdot f_{\mathrm{exc}}) - Y_M(k \cdot f_{\mathrm{exc}}, j)]. \tag{16}$$

FSP-ILC performance is relatively close to those of P-ILC. The main advantage of the former is its ability to ignore all the high-frequency components ($>Mf_{\mathrm{exc}}$), including white noise and power source oscillations, especially when f_{exc} is low. Its main drawback is the two Fourier transforms and the sum of complex numbers required per iteration, slowing down the control speed and inducing limitations in the low-frequency range. The computation time can be reduced significantly if a fast Fourier transform (FFT) is employed, but with the additional restriction that the number of samples in the waveform becomes a power of 2.

3) Phase Correction by Determination of Measure-Goal Delay: P-ILC performances depend on the power supply dynamic response and capability to generate x without undesired phase lag. A phase correction is sometimes needed to increase the feedback performance. For this, several methods have been proposed, including phase correction by determination of measure-goal delay (PhC-MGD), a technique described by Stupakov *et al.* [21]. In this method, a preliminary step increases x until y_M reaches the required amplitude. This operation is achieved by a P-ILC correction of gain modulated by $\mathrm{y_M}$'s amplitude identified at the previous stage [(17)]

$$x(t, j+1) = x(t, j) \cdot \left\{1 + \frac{K_P \cdot [\max(y_G) - \max(y_M(j))]}{\max(x(j))}\right\}. \tag{17}$$

Once y_M reaches the required threshold, x is recalculated through a sum of two weighted contributions (G_{ph} is the weight), the corrected phase contribution x_{ph} and the corrected amplitude contribution x_{ampl}

$$x(t, j+1) = G_{\mathrm{ph}} \cdot x_{\mathrm{ph}}(t, j+1) + \left(1 - G_{\mathrm{ph}}\right) \cdot x_{\mathrm{ampl}}(t, j+1) \tag{18}$$

where x_{ph} is calculated as follows.

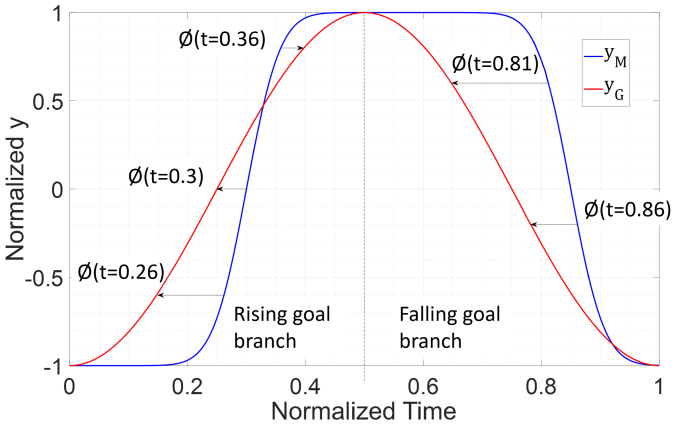

Fig. 2. PhC-MGD delay illustration.

1) The measure is normalized according to the targeted waveform

$$y_M = y_M \cdot \frac{\max(y_G).}{\max(y_M)}. \tag{19}$$

1) The resulting signal is divided into sections where the targeted waveform is monotonic.
2) The delay $\phi(t)$ (see Fig. 2) between the targeted waveform and the measurement is estimated.
3) $\phi(t)$ is applied simultaneously to y_M and x and leads to the delayed versions y_{req} and x_{ph}

$$\begin{cases} x_{\text{ph}}(t, j+1) = x(t+\phi(t), j) \\ y_{\text{req}}(t, j+1) = y_M(t+\phi(t), j). \end{cases} \tag{20}$$

X_{ampl} is obtained from a P-ILC method of y_{req} targeted waveform instead of the usual y_G

$$x_{\text{ampl}}(t, j+1) = x(t, j) + K_P \cdot \left[y_{\text{req}}(t, j) - y_M(t, j)\right]. \tag{21}$$

In [21], G_{ph} has a nonzero value exclusively in the high-frequency range when phase shift exists. The main drawback of PhC-MGD is the normalization step, which flattens the measurement signal in the presence of undesired noise peaks and makes the phase delay estimation complicated. This noise issue has been solved partially in [21] by taking 1000 points per cycle, interpolating H_{surf} with a cubic spline, and smoothing B_a with a numerical filter.

4) Phase Correction by P-ILC on Angles (PhC-P-ILC): In 2005, Zurek *et al.* [40] proposed a correction method described as the combination of two steps.

1) An amplitude correction leading to x_* (an intermediary variable) and assimilated to a P-ILC of effective gain inversely proportional to y_M amplitude

$$X_*(t, j+1) = x(t, j) + K_P \frac{\epsilon(t, j)}{\max(y_M(j))} \tag{22}$$

$$\mathrm{x}_*(t, j+1) = x(t, j) + \frac{K_P}{\max(y_M(j))}[y_G(t) - y_M(t, j)]. \tag{23}$$

2) A phase correction applied through a phase delay function F

$$x(t, j+1) = F[x_*(t, j+1)]. \tag{24}$$

During this phase correction, every involved quantity is expressed by its Fourier series [(25)–(28)]

$$y_M(t, j) = a_0 + \sum_{k=1}^{M} a_k(j) \sin[2\pi k f_1 t + \phi_k(j)] \tag{25}$$

$$y_G(t) = b_0 + \sum_{k=1}^{M} b_k \sin[2\pi k f_1 t + \psi_k] \tag{26}$$

$$x_*(t, j) = c_0 + \sum_{k=1}^{M} c_k(j) \sin[2\pi k f_1 t + \theta_k(j)] \tag{27}$$

$$I(t, j) = d_0 + \sum_{k=1}^{M} d_k(j) \sin[2\pi k f_1 t + \beta_k(j)] \tag{28}$$

where M is the number of considered harmonics, f_1 is the targeted waveform frequency, a_i, b_i, c_i, and d_i are the Fourier amplitudes, and I is the output current. I and x are linked through (29). They are identical if the source is an ideal unity gain amplifier ($G_{\text{source}} = 1$)

$$I(t, j) = G_{\text{source}}(s) \cdot x(t, j). \tag{29}$$

ϕ_i, ψ_i, θ_i, and β_i are the Fourier phase lags associated with a_i, b_i, c_i, and d_i, respectively. With this formalism

$$\begin{aligned} x(t, j+1) &= F[x_*(t, j+1)] \\ &= \sum_{k=0}^{M} c_k(j+1) \cdot \sin[2\pi k f_1 t + \theta_k(j+1) + \alpha_k(j+1)] \end{aligned} \tag{30}$$

and

$$\alpha_k(j+1) = \alpha_k(j) + K_\alpha \cdot (\psi_k - \beta_k(\mathrm{j})) \tag{31}$$

where α_k is the kth harmonic applied phase lag, and K_α a proportional gain. PhC-P-ILC reduces the influence of the power source but works in the Fourier domain, which means time-consuming direct and inverse transformations (especially when the number of considered data points is large). The implementation is complex compared with P-ILC.

5) Nonlinear Correction With a Quasi-Newtonian Method: In 2008, Yamamoto and Hanba [41] described the quasi-Newtonian method (QNM), a nonlinear iterative control method derived from the BFGS-like technique published by Li and Fukushima [42], a few years before. The Broyden–Fletcher–Goldfarb–Shanno (BFGS) algorithm can be described as a line search optimization method, and Li's method is the derivative-free version of this algorithm.

At each iteration, several variables need to be evaluated: an $N\cdot$ Hessian matrix B_j (where N is the size of vector x), y_M, y_G, and ϵ_M

$$\epsilon_M(t, j) = f[x(t, j)]. \tag{32}$$

B_0 (initialization at $j = 0$) is defined as an identity matrix, and f is a function to minimize. For each iteration j, the following algorithm is run.

1) The search direction p_j is found by solving

$$B_{j-1} \cdot p_j = -\epsilon_{M_{j-1}}. \tag{33}$$

2) The step-size α_j is set to 1, and a new measure is made with

$$x_{\text{temp}} = x_{j-1} + \alpha_j \cdot p_j \tag{34}$$

which leads to obtaining $y_{M_{\text{temp}}}$ and ϵ_{temp}.

3) If the error is not small enough ($\|\epsilon_{M_{\text{temp}}}\| > \rho \cdot \|\epsilon_{M_{j-1}}\| - \sigma_2 \cdot \|p_j\|^2$), the previous step is repeated, but α_j is contracted by a factor $\beta \in [0\text{–}1]$

$$\alpha_j = \beta \cdot \alpha_j. \tag{35}$$

This step is repeated until ($\|\epsilon_{M_{\text{temp}}}\| > (1+\eta_j) \cdot \|\epsilon_{M_{j-1}}\| - \sigma_1 \cdot \|\alpha_j \cdot p_j\|^2$).

4) B_j is updated according to the following equation:

$$B_j = B_{j-1} + \theta_j \cdot \frac{\left(\epsilon_{\text{temp}} - \epsilon_{j-1}\right) - B_{j-1} \cdot \left(x_{\text{temp}} - x_{j-1}\right)}{\|\epsilon_{\text{temp}} - \epsilon_{j-1}\|^2} \cdot \left(x_{\text{temp}} - x_{j-1}\right)^{\text{T}} \tag{36}$$

where θ_j is set to ensure B_j is not singular.

6) x_j and y_j are set from the temporary variables: $x_j = x_{\text{temp}} \text{and} y_j = \text{y}_{\text{temp}}$.

QNM differs from [42] by a different initialization of α_j

$$\alpha_j = \frac{1}{1 + \|\epsilon_{j-1}\|}. \tag{37}$$

QNM converges faster than P-ILC, especially near saturation, where P-ILC requires hundreds of iterations. However, QNM suffers from several weaknesses, including the excessive number of parameters: the fixed parameters ρ, β, $\bar{\theta}$, σ_1, and σ_2, and the variable ones such as η and θ modified for every iteration

$$\sum_{k=0}^{+\infty} \eta_j < \eta < \infty \tag{38}$$

$$|\theta_{j-1} - 1| < \overline{\theta}. \tag{39}$$

Another drawback is the computationally expensive inversion of square matrix. Convergence speed is also impacted by the multiple measurements needed per iteration. Hence, QNM is inadequate in the very-low-frequency range.

6) Least-Square Method for a $H_{\text{surf}}(B_a)$ Polynomial Identification: In 2011, Anderson [43] proposed the least-square method for a $H_{\text{surf}}(B_a)$ polynomial identification (LSM-PI), an alternative iterative method that can be summarized as follows.

1) Like in PhC-MGD, the dataset y_M is divided into monotonic sections, and an offset is applied to obtain $x(y_M = 0) = 0$ for each section.

2) $X(y_M)$ is defined for every section and approximated by a high-order polynomial (up to the order of 30 in [40])

$$x(y_M) \approx \sum\nolimits_{i=1}^{30} a_i \cdot y_M^i(t). \tag{40}$$

3) a_i coefficients are determined with a least-squares method, and a phase term is considered for the hysteretic behavior.

4) x is calculated from (40) by replacing y_M by y_G [(41)]

$$x(t) = \sum_{i=1}^{30} a_i \cdot y_G^i(t). \tag{41}$$

This method converges with a minimal number of iterations (just three as claimed in [43]), but its performance relies heavily on the order of the polynomial function. Many oscillation issues are noticed. [Especially near saturation, where the magnetic permeability μ is low, but the $H_{\text{surf}}(B_a)$ slope is high.] The least-squares optimization is computationally expensive, especially if many sampling points are considered. This problem can be lessened by expressing $H_{\text{surf}}(B_a)$ in a different orthonormal system. Moreover, this method assumes that $H_{\text{surf}}(B_a)$ is bijective, which is not the case if the maxima of H_{surf} and B_a are not simultaneous (as it is in the high-frequency range). In that case, a phase delay must be considered to avoid wrong results from the least-square optimization.

7) Other Methods: It is not possible to provide an exhaustive list of all feedback methods and their modifications described in the scientific and technical literature. The main techniques introduced in the sections above have been numerically implemented and tested in this study. They have been chosen for their singularities and originalities, but more methods exist, and even if neither detailed nor tested, they are worth mentioning in this article.

1) In 2016, Zhang *et al.* [44] described a proportional corrector, working in the frequency domain and in which both magnitudes and phases are corrected. For every harmonic, the correction can be written as

$$X_{\text{mag}} = K_{P_{\text{mag}}} \cdot \left[Y_{G_{\text{mag}}} - Y_{M_{\text{mag}}}\right] + K_{I_{\text{mag}}} \cdot \int \left(Y_{G_{\text{mag}}} - Y_{G_{\text{mag}}}\right) \text{d}t \tag{42}$$

$$X_{\text{ph}} = K_{P_{\text{ph}}} \cdot \left[Y_{\text{G}_{\text{ph}}} - Y_{M_{\text{ph}}}\right] + K_{I_{\text{ph}}} \cdot \int \left(Y_{G_{\text{ph}}} - Y_{M_{\text{ph}}}\right) \text{d}t. \tag{43}$$

Then, $x(t,\ j+1)$ is written as a Fourier series thanks to the X_{mag} and X_{ph} coefficients. This method shares the same strengths and weaknesses as FSP-ILC but is also very sensitive to the nonlinear behavior of the ferromagnetic sample. In [44], this issue is solved by correcting the calculated phases based on a lookup table. Unfortunately, no details are provided about the method for constructing such a lookup table.

2) White *et al.* [45] use a proportional derivative PD-ILC method to control the excitation current I (assuming that H_{surf} is proportional to I and the resistances and inductances values are perfectly known). Good results are obtained, but compared with P-ILC, the implementation is complex and requires detailed knowledge of the experimental conditions and their evolution during the test, which is not trivial considering that the inductance varies significantly with the level of excitation.

3) Bosack *et al.* [46] start from Jiles–Atherton's model and assume the magnetization M can be written as

$$\frac{\text{d}M}{\text{d}t} = g(H_{\text{surf}}, M, t) + f(H_{\text{surf}}, M, u) \tag{44}$$

where f and g are the two known functions, and u is a control variable, defined by

$$\frac{\mathrm{d}H_{\mathrm{surf}}}{\mathrm{d}t} = \frac{\mathrm{d}H_0}{\mathrm{d}t} + \frac{\mathrm{d}H_c}{\mathrm{d}t} = \frac{\mathrm{dH}_0}{\mathrm{d}t} + u \tag{45}$$

where H_0 is the ambient field excitation, and H_c is the corrected contribution. The resolution of the system gives

$$u = -\frac{\mathrm{d}H_0}{\mathrm{d}t} - K_P \cdot f(M) \cdot z\big(M - M_{\mathrm{goal}}\big). \tag{46}$$

Equation (46) looks like a K_p proportional correction. No details about the practical implementation are given in [46], except the use of a real-time PID corrector. The estimations of f and g rely on identification steps, and calibration must be made each time the whole system changes, which can be time-consuming, especially if recalibration is to be applied at each new measurement frequency. Finally, nonlinear algorithms have also been described in contexts unrelated to magnetic waveform control (electrohydraulic molding machine in [47] or lithographic apparatus in [48]). Like QNM, these methods require matrices inversion, limiting the experimental sampling rate and leading to feedback control incompatible with $\mathrm{MBN}_{\mathrm{energy}}$ characterizations.

C. Required Precision Criterion

All the methods described in this section have been developed to comply with international magnetic characterization standards, and different criteria have been proposed for their validation. It is worth noting that some of these criteria apply to the time derivative z of the targeted waveform x.

These criteria include the following.

1) The relative Euclidean difference is

$$d_{\mathrm{red}}(x, y) = \sqrt{\frac{\int [x(t) - y(t)]^2 \mathrm{d}t}{\int x(t)^2 \mathrm{d}t}}. \tag{47}$$

2) The form factor (applied only to z. It is worth noting that z criteria are particularly difficult to meet, as any minor distortion in x gets amplified due to the derivative) is

$$\mathrm{FFD}\big(z, y'\big) = \big|\mathrm{FF}(z) - \mathrm{FF}\big(y'\big)\big| = \left|\frac{\mathrm{RMS}(z)}{\mathrm{AVG}(|z|)} - \frac{\mathrm{RMS}(y')}{\mathrm{AVG}(|y'|)}\right|. \tag{48}$$

3) The Pearson coefficient is

$$d_{\mathrm{pearson}}(x, y) = \frac{\int [y(t) - \mathrm{AVG}(y)][x(t) - \mathrm{AVG(x)}]\mathrm{dt}}{\sqrt{\int [y(t) - \mathrm{AVG}(y)]^2 \mathrm{d}t \int [x(t) - \mathrm{AVG}(x)]^2 \mathrm{d}t}}. \tag{49}$$

4) The total harmonic distortion (applied only to z) is

$$\mathrm{THD}(z) = \frac{\sqrt{\sum_{k=2}^{+\infty} z_k^2}}{z}. \tag{50}$$

5) The amplitude error is

$$\mathrm{AE}(x, y) = \frac{(x_{\max} - x_{\min}) - (y_{\max} - y_{\min})}{x_{\max} - x_{\min}}. \tag{51}$$

TABLE I
ACCURACY CRITERIA OF THE METHODS DESCRIBED IN THIS SECTION

Source	Euclidean Difference	Form Factor	Pearson Coefficient	Other
[24] P-ILC				Amplitude error < 0.2%
[41] QNM		1.11 ± 1%		Distortion < 1%
[43] LSM-PI		1.11 ± 0.1%		THD < 0.1%
[21] PhC-MGD		1.11 ± 0.1%	> 1 - 10^{-5}	Amplitude error < 0.1%
[44]	< 0.3% (magnitudes and phases)			
[40] PhC-P-ILC		1.11 ± 1%		THD < 1%; Amplitude error < 0.1%

Table I provides the target values as applied in the literature. Even if different waveforms can have the same form factor [20], [41], the IEEE standards recommend the use of this criterion for the magnetic hysteresis and losses characterization [49], [50]. It is unsurprising to find it applied in many studies. For the $\mathrm{MBN}_{\mathrm{energy}}$ characterization, we found it relevant to apply the following criteria.

1) Relative Euclidean difference $< 0.5\%$.
2) z form factor $= F_{\mathrm{goal}} \pm 0.5\%$.
3) Pearson coefficient $>$ 1–3 $\times$ 10^{-5}.
4) z THD $< 0.5\%$.

III. NUMERICAL IMPLEMENTATION

In our quest toward the "best" iterative method for $\mathrm{MBN}_{\mathrm{energy}}$ hysteresis cycles, characterization, and STL application, all the techniques described in Section II have been numerically implemented using MATLAB[1]. A sigmoid-type anhysteretic behavior [(52)] has been used to simulate the material's answer

$$y_M(t, j) = f[x(t, j)] = \frac{2}{\pi} \arctan[x(t, j)]. \tag{52}$$

Equation (52) is convenient as saturation is taken into account, and x_G can be expressed analytically

$$x_G(t) = \tan\left(\frac{\pi}{2} y_G(t)\right). \tag{53}$$

The objective is to find x_G leading to a sinusoidal y_G. A preliminary test consists in plotting the spectral content of x_G as a function of y_G amplitude (Fig. 3).

When y_G amplitude is large, high amplitude harmonics are generated, triggering issues if the power source dynamic performance is limited. Waveform control is easier at low amplitude (no saturation and quasi-linear material behavior). THD of x_G can reach 0% at very low amplitudes, and it, however, increases up to 18% at 0.75· max(y_G) and even 51% at 0.95· max(y_G). THD values exceeding 100% are possible if no control is applied [20], and this is expected to occur for even deeper saturation. No noise has been considered in all the following tests. The power amplifier is supposed to be ideal (infinite bandwidth), with perfect impedance matching. The sampling frequency has been reduced to 500 Hz to limit the memory allocation and reach convergence even with QNM.

[1]Registered trademark.

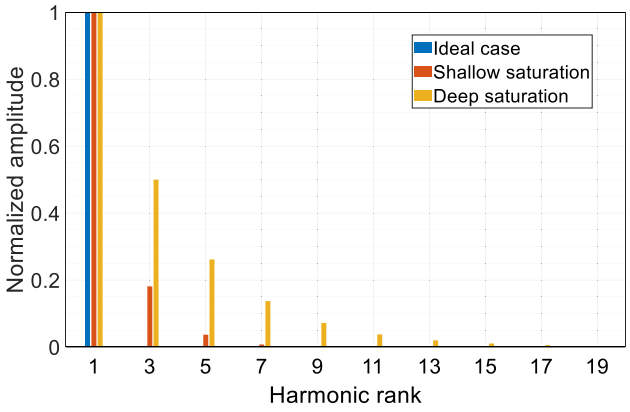

Fig. 3. x_G harmonic content versus y_G amplitude.

TABLE II
SHALLOW SATURATION SIMULATION PARAMETERS

	Parameters
P-ILC, FDP-ILC	$k_P = 2.77$
FSP-ILC	$k_P = 2.77$, $N_{HARMONICS} = 200$
PhC-P-ILC	$K_P = 4.4$, $k_\alpha = 0$
PhC-MGD	$G_{PH} = 0$, $K_P = 1$
QNM	Same parameters as in [29], except $\lambda = 0.5$ and $\beta = 0.6$
LSM-PI	$N_{POWERS} = 45$

A. Shallow Saturation

The tested methods are first compared in a shallow saturation case

$$y_G(t) = 0.75 \sin(2\pi t). \tag{54}$$

The simulations are stopped when the relative Euclidean difference or the form factor difference falls below 10^{-10}. The maximum iteration number is set to 600. On the one hand, such low error is only achievable in simulation; experimental conditions are affected by white noise and drifts. On the other hand, such high accuracy allows testing the methods with y_M extremely close to y_G. Table II gives the simulation parameters, and Fig. 4 shows the simulation results.

Convergence is obtained for all the methods tested. LSM-PI and PhC-MGD are the fastest, with approximately ten iterations. Still, for both these methods, the amplitude correction step requires a lot of intermediary measurements, which can be problematic in the low-frequency range. QNM converges after 40 iterations but needs long calculation times. P-ILC follows with around 60 iterations and minimal calculation times. Finally, FSP-ILC converges after almost 180 iterations. It is worth noting the residual error on P-ILC and FSP-ILC inherent to those methods and impossible to remove. Table III concludes this first set of tests by comparing the methods based on the criteria described in Section II-A:

Table III "calculation time" only considers the waveform identification computation time, i.e., it does not include additional times associated with virtual measurement simulation

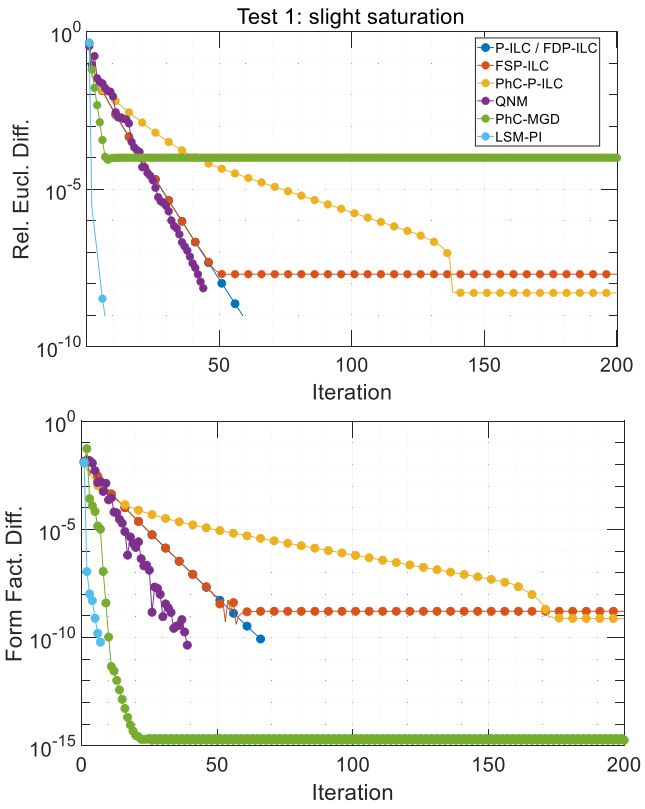

Fig. 4. Relative Euclidean and form factor differences for the shallow saturation test.

TABLE III
PERFORMANCE COMPARISON FOR THE SHALLOW SATURATION TEST

	Num. of iter.	**Num. of meas.**	**Fin. rel. euc. diff.**	**Final form factor**	**Calc. time per iter. (s)**	**Total calc. time (s)**
P-ILC	66	66	$< 10^{-10}$	$8.9 \cdot 10^{-10}$	$4.7 \cdot 10^{-4}$	0.031
FDP-ILC	66	66	$< 10^{-10}$	$8.9 \cdot 10^{-10}$	$4.2 \cdot 10^{-4}$	0.023
FSP-ILC	60	60	$2.5 \cdot 10^{-8}$	$1.6 \cdot 10^{-9}$	0.008	0.47
PhC-P-ILC	174	174	$2.2 \cdot 10^{-9}$	$7.6 \cdot 10^{-10}$	0.01	1.7
PhC-MGD	11	196	$9.9 \cdot 10^{-5}$	$< 10^{-10}$	0.031	0.338
QNM	40	90	$1.4 \cdot 10^{-8}$	$< 10^{-10}$	0.52	20.92
LSM-PI	7	192	$9.0 \cdot 10^{-10}$	$< 10^{-10}$	0.39	2.743

(equivalent to the measurement time in the experimental setup).

B. Deep Saturation

In the next test, the iteration methods are tested closer to a fully saturated configuration, where larger nonlinearity is present

$$y_G(t) = 0.95 \sin(2\pi t). \tag{55}$$

The maximum iteration number is raised to 1500 since overall convergence is slower in this case. Fig. 5 shows the simulation results, and Table. IV lists the simulation parameters.

Again, QNM and PhC-MGD show the fastest convergence speed. PhC-P-ILC is also very fast, outclassing QNM and

TABLE IV
DEEP SATURATION SIMULATION PARAMETERS

	Parameters
P-ILC, FDP-ILC	$k_P = 3$
FSP-ILC	$k_P = 3$, $N_{HARMONICS} = 200$
PhC-P-ILC	$K_P = 5.6$, $k_\alpha = 0$
PhC-MGD	$G_{PH} = 0$, $K_P = 0.4$
QNM	Same parameters as in [29], except $\lambda = 0.5$ and $\beta = 0.5$
LSM-PI	$N_{POWERS} = 70$

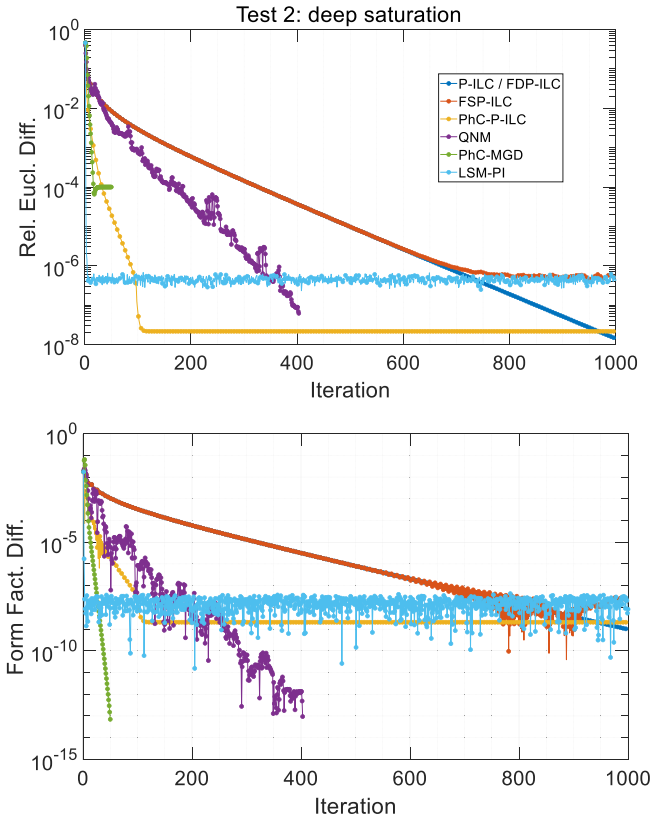

Fig. 5. Relative Euclidean and form factor differences for the deep saturation test.

exhibiting temporary convergence errors. P-ILC converges slowly for this test, but unlike PhC-P-ILC, it never gets stuck on a precision plateau. Table V lists the comparison of the performances. The precision criterion is set to $<10^{-7}$.

A high number of iterations limits LSM-PI and PhC-MGD performances. QNM's iteration number is lower, but each requires a significant calculation time. The PhC-P-ILC method converges with a reduced number of iterations, eight times lower than P-ILC, but the calculation time for the latter is extremely short.

C. Overall Simulation Results

Table VI compiles the comparisons based on the performance criteria defined in Section II-A.

TABLE V
PERFORMANCE COMPARISON FOR THE DEEP SATURATION TEST

	Num. of iter.	Num. of meas.	Fin. rel. euc. diff.	Final form factor	Calc. time per iter. (s)	Total calc. time (s)
P-ILC	653	653	$1.29\cdot10^{-6}$	$< 10^{-7}$	$2.7\cdot10^{-4}$	0.176
FDP-ILC	653	653	$1.29\cdot10^{-6}$	$< 10^{-7}$	$4.2\cdot10^{-4}$	0.272
FSP-ILC	637	637	$1.69\cdot10^{-6}$	$< 10^{-7}$	0.009	5.97
PhC-P-ILC	87	87	$9.97\cdot10^{-7}$	$< 10^{-7}$	0.012	1.02
PhC-MGD	24	3182	$9.78\cdot10^{-5}$	$< 10^{-7}$	0.19	4.61
QNM	179	484	$9.57\cdot10^{-5}$	$< 10^{-7}$	0.49	88.8
LSM-PI	3	3161	$2.03\cdot10^{-6}$	$< 10^{-7}$	2.21	6.63

TABLE VI
PERFORMANCES COMPARISON BASED ON THE PERFORMANCE CRITERIA DEFINED IN SECTION II-A

	Num. of var.	Exec. time (per iter.)	Conv. speed	Precision	Achiev. samp. Freq.	Robustness
P-ILC / FDP-ILC	**1**	**Low**	Low-Med.	**High**	**High**	**High**
FSP-ILC	**1**	Med.	Low-Med.	Med.	**High**	**High**
PhC-P-ILC	2	Med.	Med.	**High**	**High**	**High**
PhC-MGD	2	Med.	**High**	**High**	Med.	Low
QNM	6	High	**High**	**High**	Low	Low
LSM-PI	N	Very high	**High**	**High**	Med.	Low

MBN_{energy} measurements require high sampling frequency, up to several hundreds of kilohertz, and long-time measurements leading to huge memory size for numerical feedback variables. Methods that rely on matrix inversions like QNM or parameter optimization like LSM-PI are unsuitable. This issue can be partially solved by downsampling the signals, applying correction, and upsampling the resulting waveforms by interpolation (PhC-MGD [21]). However, it means complexity and uncertainty in the measurement treatment. White noise's consequence on the working signals is another issue to consider. Methods like PhC-MGD require an intense averaging process to reach convergence which means extended time acquisition (several cycles) or a sliding window filter. These treatments bring complexity in the signal processing and potentially additional phase delays. Since B_a is obtained by integrating a noisy signal, a drift is always expected. Such a drift can be problematic on methods that normalize signals or expect y_M to have a specific amplitude (PhC-MGD and LSM-PI). A pretreatment of B_a is required to reach convergence. Oppositely, P-ILC does not require a perfect drift compensation to reach convergence. After all the numerical tests performed in this study, and based on Table VI analysis, P-ILC appears to be the most adapted method in the context of the $MBN_{energy}(H_{surf})$ hysteresis cycles characterization. In Section IV, improvements are proposed for even better and faster convergence.

IV. P-ILC EXTENSIONS

P-ILC is an excellent method for magnetization control digital feedback. P-ILC is simple to implement and tune. It is

robust and fast. Its only limitation comes from the convergence speed, especially near saturation when the permeability falls and where a weak variation of H_{surf} generates an even lower variation of B_a. This problem can be partially solved by increasing the proportional gain, but the response will diverge in the high permeability zones. A better solution consists in modulating K_p according to the system answer

$$x(t, j+1) = x(t, j) + K_P(t, j)\epsilon(t, j). \tag{56}$$

This method requires additional parameters and should be considered with special attention. It can be implemented from an error array based on the two previous iterations (P-ILC-2 [51]) and give the following equation:

$$x(t, j+2) = x(t, j+1) + K_{P1}\epsilon(t, j+1) + K_{P2}\epsilon(t, j). \tag{57}$$

The resulting error becomes a weighted sum of $j+1$ and j errors iterations. A generalized version (P-ILC-N) considering all the previous state N can even be written by extending (57)

$$x(t, j+N) = x(t, j+N-1) + \sum_{q=1}^{N} K_{P_q}\epsilon(t, j+N-q). \tag{58}$$

P-ILC-N convergence is faster. It is also more robust than standard P-ILC [51]. However, a minimum of N measurements are necessary for the corrector to be fully working. All K_{Pq} coefficients need to be optimized individually, which can be complex and demanding in experimental data. Hence, N should be kept as small as possible unless a reliable model is available for simulation. Another possibility consists of structuring the P-ILC iterative law as a Taylor approximation. (Assuming x is a y smooth function.)

$$x(y_G) = x(y_M) + A(y_M)(y_G - y_M). \tag{59}$$

If $x(t, j+1) = x_G(t)$, higher orders Taylor approximation gives P-ILC-TA, as given in the following equation:

$$x(t, j+1) = x(t, j) + \sum_{s=1}^{N} K_{Ps}\epsilon(t, j)^s. \tag{60}$$

It is also possible to replace A in (59) with its optimal value, as obtained by the Taylor's approximation (P-ILC-TD)

$$x(y_G) = x(y_M) + \frac{dx}{dy}(y_M)(y_G - y_M) \Rightarrow \frac{dx}{dy} = \frac{1}{\frac{dy}{dx}} \propto \frac{1}{\mu} \tag{61}$$

$$\Rightarrow K_P(t, j) = \frac{dx}{dy_M}(t, j). \tag{62}$$

P-ILC-TD can reach high-speed convergence rates. K_p being inversely proportional to the system reactivity, the correction will be significant when dy_M/dx is small. However, relying on derivatives, P-ILC-TD requires exact measurement, no noise, delays, or bandwidth limitations. Otherwise, this method diverges very quickly. Finally, the deep saturation test (Section III-B) was repeated, and all P-ILC new variants were tested. Fig. 6 shows the simulation results, and Table VII shows the corresponding iteration numbers.

TABLE VII
COMPARATIVE RESULTS BASED ON THE ITERATION NUMBER BEFORE CONVERGENCE

	Number of iterations
P-ILC	2135
P-ILC-TA (7th degree)	1835
P-ILC-3	979
P-ILC-9	613
P-ILC-TD	55

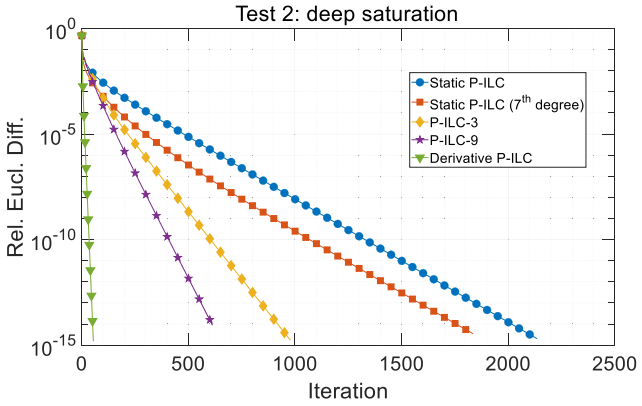

Fig. 6. Relative Euclidean differences and deep saturation test for the different P-ILC methods.

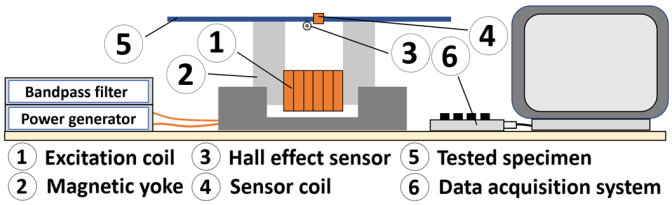

Fig. 7. Overall 2-D view of the Barkhausen noise experimental setup.

All alternative methods converge faster than P-ILC. P-ILC-TD outclasses all the proposed methods. An iterative process close to P-ILC-TD robust enough to handle white noise would be by far the most indicated method.

V. EXPERIMENTAL SETUP AND IMPLEMENTATION

The experimental setup used for the Barkhausen noise characterization has been precisely described in [19]. The excitation of the sample is based on single C-yoke with the magnetizing winding, and with the sensors attached to the sample under test. An overall 2-D view of this experimental setup is depicted in Fig. 7.

The power amplifier was a Kepco BOP100-10MG. The excitation coil was made out of 10 turns. The studied specimens were all grain-oriented electrical steels (FeSi GO 3wt%, M140-27). Their dimensions were 280 × 30 × 0.3 mm^3, with the length in the easy magnetization direction. Two 120 turns' coils were wound around the specimen and plugged in opposite directions as recommended in [52]. The distance separating the sensor coils was set arbitrarily to 10 mm,

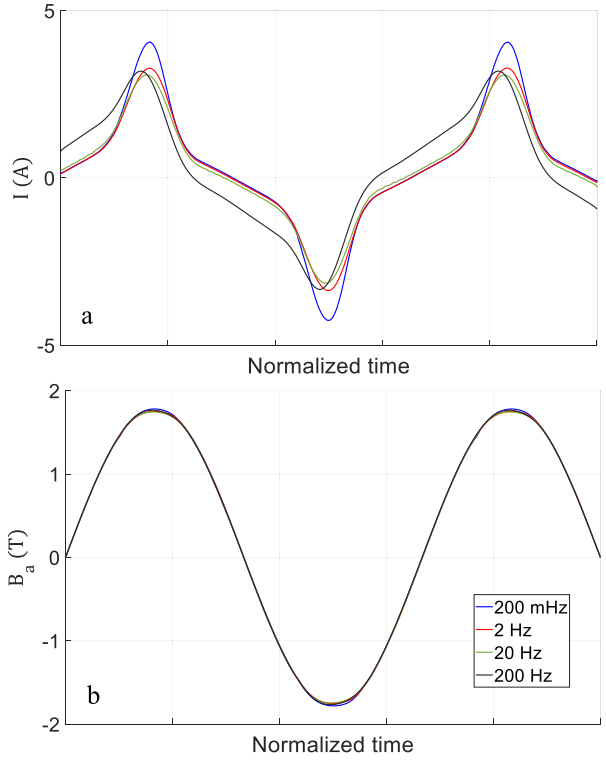

Fig. 8. (a) $I(t)$ experimental waveforms. (b) $B_a(t)$ experimental waveforms.

TABLE VIII

EXPERIMENTAL PERFORMANCES COMPARISON BASED ON THE ACCURACY CRITERIA DEFINED IN SECTION II-C

	200 mHz	2 Hz	20 Hz	200 Hz	Goal (Int. stand.)
Euc. Dist. (%)	0.678	0.35	0.57	0.34	< 0.5
Pears. Coef.	0.9999897	0.99999394	0.9999841	0.99999438	> 0.99997
Form Fact. Diff. (dB/dt)(%)	0.74	0.29	0.14	0.31	< 0.5
Amp. Diff. (%)	0.96	0.27	0.05	0.3	< 1
THD (dB/dt) (%)	5.33	1.4	2.95	3.7	< 0.5

Criteria met Criteria not met

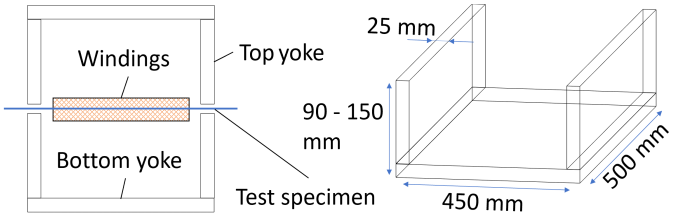

Fig. 9. IEC 60404-3 single sheet tester illustration and yoke dimensions.

as used in the previous work [19], [53], [54] by the authors. The influence of this distance has not been investigated in detail. Two Krohn-Hite 3362 amplifiers-filters were used for the signal conditioning and a National Instruments DAQ USB-6346 acquisition card, controlled through a GUI in Python and of 500-kHz sampling frequency for their acquisitions. Python and MATLAB were used for the numerical treatment. Equations (63)–(65) summarized all the tests carried out

$$B_a(\text{goal}) = B\sin(2\pi f_{\text{exc}} t) \tag{63}$$

$$B = 1.8\text{T} \tag{64}$$

$$f_{\text{exc}} = \{0.2, 2, 20, 200\}\ \text{Hz}. \tag{65}$$

P-ILC was used to set the current waveforms. Fig. 8 depicts the experimental results obtained on three decades of frequency and B_a equal to 1.8 T, i.e., the worst case analyzed a scenario in terms of nonlinear behavior.

The 200-MHz current peak is unexpectedly high as compared with other frequencies. However, this difference could be caused simply by the nonlinearity of the magnetic material because of the larger difference in amplitude as evident from Table VIII. Table VII summarizes the accuracy of the experimental results by comparing them using sub-Section II-C criteria.

Some experimental results (Fig. 8) do not reach the accuracy targeted by the international standards. On the one hand, these standards imposed tight specifications of the experimental conditions (geometry and measurements), far from the experimental setup depicted in Fig. 7. IEC 60404-3 [50] related to the single sheet tester imposed by instant to use a top and a bottom yoke of large dimensions as displayed in Fig. 9.

On the other hand, the setup (Fig. 7) has been designed based on usual MBN observation methods, like in a non-destructive testing context where magnetization waveform control is not required and never done (see [55], [56], [57], [58], [59]). This setup delivers magnetic excitation significantly less homogeneous compared with those of [50], and the volume of the tested specimen is reduced. These limitations result in a considerable increase in the magnetization control complexity, justifying a lower accuracy in Table VIII results.

A phase delay was also noticed between $I(t)$ and $B_a(t)$. This delay could be a source of divergence for some ILC algorithms [like QNM, whose core assumption relies on the $I(B_a)$ bijectivity]. Finally, Fig. 10 shows, as examples, the 20-Hz, 1.8-T sinus flux density, $B_a(H_{\text{surf}})$, and $\text{MBN}_{\text{energy}}(H_{\text{surf}})$ measured cycles. Differences can be observed between the experimental $\text{MBN}_{\text{energy}}(H_{\text{surf}})$ and the $B_a(H_{\text{surf}})$ hysteresis cycles. Those differences were expected and can be explained as follows.

1) All magnetization contributions are involved in the $B_a(H_{\text{surf}})$ hysteresis cycles, mainly the domain wall motions and the magnetization rotation.
2) For the $\text{MBN}_{\text{energy}}(H_{\text{surf}})$ cycle, the contribution is limited to the domain wall motions.

It is worth noting the difference at saturation once the cycle is closed. On the one hand, the $\text{MBN}_{\text{energy}}(H_{\text{surf}})$ cycle reaches a flat saturation. No more variation of the $\text{MBN}_{\text{energy}}$ is observed, reflecting the entire disappearance of the domain wall motions. On the other hand, the $B_a(H_{\text{surf}})$ still varies. The magnetization rotation remains active and increases the magnetic flux density. The differences are expected to be even more pronounced in

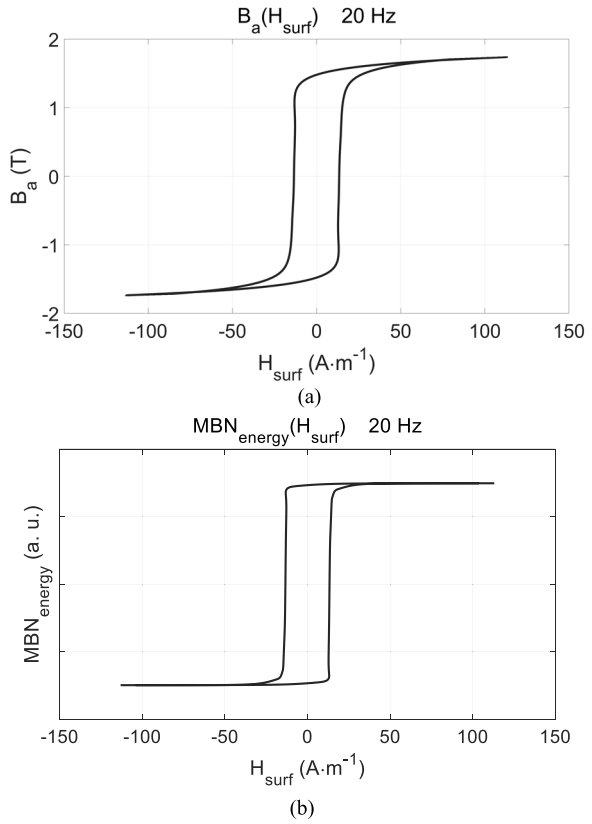

Fig. 10. (a) $B_a(H_{\text{surf}})$ experimental hysteresis cycle. (b) $\text{MBN}_{\text{energy}}(H_{\text{surf}})$ renormalized experimental hysteresis cycles.

the higher frequency range. When $B_a(H_{\text{surf}})$ cycles reflect all STL contributions, the $\text{MBN}_{\text{energy}}(H_{\text{surf}})$ ones are limited to the domain wall motion contributions excluding, notably, the classical loss contribution.

VI. Conclusion

Studying the magnetization mechanisms in magnetic cores is a genuine problem that has generated substantial research efforts. A fine study of the $\text{MBN}_{\text{energy}}(H_{\text{surf}})$ hysteresis cycle excitation frequency dependency and its prediction through an STL-like theory is expected to bring insights into the physical behavior of the magnetization mechanisms.

For this, the flux density has to be imposed sinusoidal from the quasi-static state up to approximately a few hundreds of hertz, depending on the nature of the tested specimen. Such control might be seen as a simple problem. Still, because of the strong linearities, the practical aspect happens to be especially complex, hence, the proliferation of the feedback algorithms in the literature (see [40], [42], [43] are good examples).

In this study, the theoretical problem of B_a control on a classic setup (yoke and sample) has been established, and the ILC (the iterative version of the classic PID controller) has been explained. Different ILC settings exist, and a detailed review of these methods was done in the second section of this article providing valuable insights generalizable to every waveform control environment. For a proper choice, the experimental conditions and the final objective have to be perfectly defined from the very beginning.

Then, six performance criteria have been proposed to identify the most adapted method in the specific context of the $\text{MBN}_{\text{energy}}(\text{H}_{\text{surf}})$ hysteresis cycle characterization, and numerical tests were performed for a comparison purpose followed by conclusions.

P-ILC gave the best performance and the highest satisfaction rate. It was therefore chosen for experimental implementation. Experimental tests were realized on a wide range of amplitude and frequency. We noticed, as expected, a more significant error for higher frequency (limitations of the practical setup bandwidth) and amplitude (stronger nonlinear behavior of the tested specimen).

References

[1] F. Fiorillo, *Measurement and Characterization of Magnetic Materials (Electromagnetism)*. New York, NY, USA: Academic, 2005.
[2] C. P. Steinmetz, "On the law of hysteresis," *Trans. Amer. Inst. Elect. Eng.*, vol. 9, no. 1, pp. 1–64, Jan. 1892.
[3] J. Reinert, A. Brockmeyer, and R. W. A. A. De Doncker, "Calculation of losses in ferro-and ferrimagnetic materials based on the modified Steinmetz equation," *IEEE Trans. Ind. Appl.*, vol. 37, no. 4, pp. 1055–1061, Jul./Aug. 2001.
[4] H. Jordan, "Die ferromagnetischen Konstanten für schwache Wechselfelder," *Elektr. Nach. Techn.*, vol. 1, p. 8, Jul. 1924.
[5] A. Krings and J. Soulard, "Overview and comparison of iron loss models for electrical machines," *J. Elect. Eng.*, vol. 10, no. 3, p. 8, 2010.
[6] F. Krall, "Analysis and implementation of algorithms for calculation of iron losses for fractional horsepower electric motors," *Sensors*, vol. 21, no. 13, p. 4392, 2021.
[7] N. P. Goss, "Electrical sheet and method and apparatus for its manufacture and test," U.S. Patent 1 965 559, Jul. 3, 1934.
[8] J. Shilling and G. Houze, "Magnetic properties and domain structure in grain-oriented 3% Si-Fe," *IEEE Trans. Magn.*, vol. MAG-10, no. 2, pp. 195–223, Jun. 1974.
[9] G. Bertotti, *Hysteresis in Magnetism: For Physicists, Materials Scientists, and Engineers*. Houston, TX, USA: Gulf Professional, 1998.
[10] G. Bertotti, F. Fiorillo, and G. P. Soardo, "The prediction of power losses in soft magnetic materials," *Le J. de Phys. Colloques*, vol. 49, no. C8, pp. C8-1915–C8-1919, Dec. 1988.
[11] K. Atallah and D. Howe, "The calculation of iron losses in brushless permanent magnet DC motors," *J. Magn. Magn. Mater.*, vol. 133, nos. 1–3, pp. 578–582, May 1994.
[12] M. Amar and R. Kaczmarek, "A general formula for prediction of iron losses under nonsinusoidal voltage waveform," *IEEE Trans. Magn.*, vol. 31, no. 5, pp. 2504–2509, Sep. 1995.
[13] J. Leicht, "Magnetic properties of electrical steel under controlled magnetisation conditions," Ph.D. dissertation, Univ. Wales, Cardiff, U.K., 2003.
[14] J. Leicht, A. J. Moses, and S. Zurek, "Hysteresis loss component under non-sinusoidal flux waveforms," *J. Magn. Magn. Mater.*, vol. 320, no. 20, pp. e608–e610, Oct. 2008.
[15] C. Ragusa, H. Zhao, C. Appino, M. Khan, O. de la Barriere, and F. Fiorillo, "Loss decomposition in non-oriented steel sheets: The role of the classical losses," *IEEE Magn. Lett.*, vol. 7, pp. 1–5, 2016.
[16] Z. Zhao and X. Hu, "Modified loss separation in FeSi laminations under arbitrary distorted flux," *AIP Adv.*, vol. 10, no. 8, Aug. 2020, Art. no. 085222.
[17] B. Ducharne, M. Q. Le, G. Sebald, P. J. Cottinet, D. Guyomar, and Y. Hebrard, "Characterization and modeling of magnetic domain wall dynamics using reconstituted hysteresis loops from Barkhausen noise," *J. Magn. Magn. Mater.*, vol. 432, pp. 231–238, Jun. 2017.
[18] B. Ducharne, B. Gupta, Y. Hebrard, and J. Coudert, "Characterization and local phenomenological model of Barkhausen noise under mechanical and magnetic excitations," in *Proc. IEEE Int. Magn. Conf. (INTERMAG)*, Apr. 2018, p. 1.
[19] P. Fagan, B. Ducharne, L. Daniel, and A. Skarlatos, "Multiscale modelling of the magnetic Barkhausen noise energy cycles," *J. Magn. Magn. Mater.*, vol. 517, Jan. 2021, Art. no. 167395.
[20] S. Zurek, *Characterisation of Soft Magnetic Materials Under Rotational Magnetisation*. Boca Raton, FL, USA: CRC Press, 2017.
[21] A. Stupakov, O. Perevertov, and V. Zablotskii, "A system for controllable magnetic measurements of hysteresis and Barkhausen noise," *IEEE Trans. Instrum. Meas.*, vol. 65, no. 5, pp. 1087–1097, May 2016.

[22] A. Stupakov and A. Perevertov, "Analog of the induction law for the magnetic Barkhausen noise," *J. Magn. Magn. Mater.*, vol. 498, Mar. 2020, Art. no. 166238.

[23] N. Grote, P. Denke, M. Rademacher, R. Kipscholl, M. Bongards, and S. Siebert, "Measurement of the magnetic properties of soft magnetic material using digital real-time current control," in *Non-Linear Electromagnetic Systems*. Amsterdam, The Netherlands: IOS Press, 1998, pp. 566–569.

[24] S. Zurek, "Practical implementation of universal digital feedback for characterisation of soft magnetic materials under controlled AC waveforms," *Przeglad Elektrotechniczny*, vol. 93, no. 7, pp. 16–21, 2017.

[25] G. Bertotti, E. Ferrara, F. Fiorillo, and M. Pasquale, "Loss measurements on amorphous alloys under sinusoidal and distorted induction waveform using a digital feedback technique," *J. Appl. Phys.*, vol. 73, no. 10, pp. 5375–5377, May 1993.

[26] G. Birkelbach, K. A. Hempel, and F. J. Schulte, "Very low frequency magnetic hysteresis measurements with well-defined time dependence of the flux density," *IEEE Trans. Magn.*, vol. MAG-22, no. 5, pp. 505–507, Sep. 1986.

[27] K. Matsubara, N. Takahashi, K. Fujiwara, T. Nakata, M. Nakano, and H. Aoki, "Acceleration technique of waveform control for single sheet tester," *IEEE Trans. Magn.*, vol. 31, no. 6, pp. 3400–3402, Nov. 1995.

[28] I. Zemánek, "Exciting signal generator for SSTs," *J. Magn. Magn. Mater.*, vols. 254–255, pp. 73–75, Jan. 2003.

[29] Y. Zhang, Y. Long, Q. Qu, R. Ye, and Y. Chang, "Precise AC magnetic measurement under sinusoidal magnetic flux by using digital feedback of harmonic compensation," *J. Magn. Magn. Mater.*, vol. 312, no. 2, pp. 443–448, May 2007.

[30] S. White, T. W. Krause, and L. Clapham, "A multichannel magnetic flux controller for periodic magnetizing conditions," *IEEE Trans. Instrum. Meas.*, vol. 61, no. 7, pp. 1896–1907, Jul. 2012.

[31] S. Baranowski, S. Tumanski, and S. Zurek, "Comparison of digital methods of the control of flux density shape," *Przeglad Elektrotechniczny*, vol. 85, pp. 93–95, Aug. 2009.

[32] H. Hollitscher, "Core losses in magnetic materials at very high flux densities when the flux is not sinusoidal," *IEEE Trans. Magn.*, vol. MAG-5, no. 3, pp. 642–647, Sep. 1969.

[33] Z. Pólik and M. Kuczmann, "Measuring and control the hysteresis loop by using analog and digital integrators," *J. Optoelectron. Adv. Mater.*, vol. 10, no. 7, pp. 1861–1865, 2008.

[34] Y. Song, Y. Gong, and S. M. Kuo, "A robust hybrid feedback active noise cancellation headset," *IEEE Trans. Speech Audio Process.*, vol. 13, no. 4, pp. 607–617, Jul. 2005.

[35] J. Lüdke and H. Ahlers, "Hybrid control used to obtain sinusoidal curve form for the power loss measurement on magnetic materials," *Mater. Sci. Forum*, vols. 373–376, pp. 469–472, Aug. 2001.

[36] H. V. Patel, S. Zurek, T. Meydan, D. C. Jiles, and L. Li, "A new adaptive automated feedback system for Barkhausen signal measurement," *Sens. Actuators A, Phys.*, vol. 129, nos. 1–2, pp. 112–117, May 2006.

[37] H. Gruebler, F. Krall, S. Leitner, and A. Muetze, "Loss-surface-based iron loss prediction for fractional horsepower electric motor design," in *Proc. 20th Eur. Conf. Power Electron. Appl. (EPE ECCE Eur.)*, Sep. 2018, p. 1.

[38] C. T. Freeman, P. L. Lewin, and E. Rogers, "Experimental evaluation of iterative learning control algorithms for non-minimum phase plants," *Int. J. Control*, vol. 78, no. 11, pp. 826–846, 2005.

[39] C. T. Freeman *et al.*, "Phase-lead iterative learning control algorithms for functional electrical stimulation-based stroke rehabilitation," *Proc. Inst. Mech. Eng. I, J. Syst. Control Eng.*, vol. 225, no. 6, pp. 850–859, 2011.

[40] S. Zurek, P. Marketos, T. Meydan, and A. J. Moses, "Use of novel adaptive digital feedback for magnetic measurements under controlled magnetizing conditions," *IEEE Trans. Magn.*, vol. 41, no. 11, pp. 4242–4249, Nov. 2005.

[41] K.-I. Yamamoto and S. Hanba, "Waveform control for magnetic testers using a quasi-Newton method," *J. Magn. Magn. Mater.*, vol. 320, no. 20, pp. e539–e541, Oct. 2008.

[42] D.-H. Li and M. Fukushima, "A derivative-free line search and global convergence of Broyden-like method for nonlinear equations," *Optim. Methods Softw.*, vol. 13, no. 3, pp. 181–201, Jan. 2000.

[43] P. Anderson, "Constant dB/dt DC characterisation through digital control of magnetic field," *Przeglad Elektrotechniczny*, vol. 87, no. 9b, pp. 77–78, 2011.

[44] C. Zhang, Y. Li, J. Li, Q. Yang, and J. Zhu, "Measurement of three-dimensional magnetic properties with feedback control and harmonic compensation," *IEEE Trans. Ind. Electron.*, vol. 64, no. 3, pp. 2476–2485, Mar. 2017.

[45] S. White, T. Krause, and L. Clapham, "Control of flux in magnetic circuits for Barkhausen noise measurements," *Meas. Sci. Technol.*, vol. 18, no. 11, pp. 3501–3510, Nov. 2007.

[46] M. Bosack, J. Kollmer, B. Niemoczynski, and S. Biswas, "Closed loop control of hysteretic magnetization," in *Proc. 7th Int. Symp. Resilient Control Syst. (ISRCS)*, Aug. 2014, pp. 1–6.

[47] H. Havlicsek and A. Alleyne, "Nonlinear control of an electrohydraulic injection molding machine via iterative adaptive learning," *IEEE/ASME Trans. Mechatronics*, vol. 4, no. 3, pp. 312–323, Sep. 1999.

[48] M. Heertjes and T. Tso, "Nonlinear iterative learning control with applications to lithographic machinery," *Control Eng. Pract.*, vol. 15, no. 12, pp. 1545–1555, Dec. 2007.

[49] *Magnetic Materials—Part 2: Methods of Measurement of the Magnetic Properties of Electrical Steel Strip and Sheet by Means of an Epstein Frame*, Standard I. 60404-2, International Electrotechnical Commission, Jun. 2008.

[50] *Magnetic Materials—Part 3: Methods of Measurement of the Magnetic Properties of Electrical Steel Strip and Sheet by Means of a Single Sheet Tester*, Standard I. 60404-3, International Electrotechnical Commission, Apr. 2010.

[51] Y. Zheng, X. Liu, J. Zhao, N. Mo, and Z. Shi, "A novel iterative learning control method and control system design for active magnetic bearing rotor imbalance of primary helium circulator in high-temperature gas-cooled reactor," *Meas. Control*, vol. 53, nos. 3–4, pp. 474–484, Mar. 2020.

[52] A. J. Moses, H. V. Patel, and P. I. Williams, "AC Barkhausen noise in electrical steels: Influence of sensing technique on interpretation of measurements," *J. Electr. Eng.*, vol. 57, no. 8, pp. 3–8, 2006.

[53] P. Fagan, B. Ducharne, L. Daniel, and A. Skarlatos, "Magnetic Barkhausen noise: A simulation tool," *AIP Adv.*, vol. 11, no. 2, Feb. 2021, Art. no. 025322.

[54] P. Fagan, B. Ducharne, L. Daniel, A. Skarlatos, M. Domenjoud, and C. Reboud, "Effect of stress on the magnetic Barkhausen noise energy cycles: A route for stress evaluation in ferromagnetic materials," *Mater. Sci. Eng., B*, vol. 278, Apr. 2022, Art. no. 115650.

[55] B. Gupta, B. Ducharne, T. Uchimoto, G. Sebald, T. Miyazaki, and T. Takagi, "Non-destructive testing on creep degraded 12% Cr-Mo-W-V ferritic test samples using Barkhausen noise," *J. Magn. Magn. Mater.*, vol. 498, Mar. 2020, Art. no. 166102.

[56] D. M. Stewart, K. J. Stevens, and A. B. Kaiser, "Magnetic Barkhausen noise analysis of stress in steel," *Current Appl. Phys.*, vol. 4, nos. 2–4, pp. 308–311, Apr. 2004.

[57] J. A. Perez-Benitez, J. Capo-Sanchez, J. Anglada-Rivera, and L. R. Padovese, "A study of plastic deformation around a defect using the magnetic Barkhausen noise in ASTM 36 steel," *NDT E Int.*, vol. 41, no. 1, pp. 53–58, Jan. 2008.

[58] M. Soto, A. Martínez-de-Guerenu, K. Gurruchaga, and F. Arizti, "A completely configurable digital system for simultaneous measurements of hysteresis loops and Barkhausen noise," *IEEE Trans. Instrum. Meas.*, vol. 58, no. 5, pp. 1746–1755, May 2009.

[59] S. Ding, G. Tian, G. Dobmann, and P. Wang, "Analysis of domain wall dynamics based on skewness of magnetic Barkhausen noise for applied stress determination," *J. Magn. Magn. Mater.*, vol. 421, pp. 225–229, Jan. 2017.

Patrick Fagan was born in Bassano del Grappa, Italy, in 1994. He received the master's degree in electrical engineering from INSA Lyon, Villeurbanne, France, in 2019. He is currently pursuing the Ph.D. degree with the CEA-LIST, Université Paris-Saclay, Gif-sur-Yvette, France, and the LGEF, INSA Lyon. The topic of the Ph.D. is the simulation of the Barkhausen noise for steel characterization and nondestructive testing (NDT).

Benjamin Ducharne received the M.S. and Ph.D. degrees in electrical engineering from the University Claude Bernard Lyon I, Villeurbanne, France, in 2001 and 2003, respectively.

In 2004, he joined the Institut Montefiore, Liège, Belgium, where he held a post-doctoral position. In 2005, he joined INSA, Lyon, France, as an Associate Professor. From 2018 to 2019, he was a Visiting Scholar and a mid-term Lecturer with Purdue University, West Lafayette, IN, USA. In 2020, he joined ELyTMaX, Tohoku University, Sendai, Japan, as a Full-Time Researcher. His main research interests are magnetic nondestructive testing, ferromagnetic and ferroelectric materials, hysteresis modeling, fractional operators, and multiphysics coupling.

Stanislaw Zurek (Senior Member, IEEE) received the M.Sc. degree from Czestochowa University of Technology, Częstochowa, Poland, in 2000, the Ph.D. degree from Cardiff University, Cardiff, U.K., in 2005, and the D.Sc. degree from Lodz University of Technology, Lodz, Poland, in 2020.

He currently holds the position of the Head of Research and Innovation, Megger Instruments, Dover, U.K.

Dr. Zurek was a fellow of IET in 2022.

Mathieu Domenjoud received the M.Sc. degree in electrical engineering from the François-Rabelais University, Tours, France, in 2008, and the Ph.D. degree in electrical engineering, with a focus on the characterization of electroacoustic properties of piezoelectric structures under electrical and mechanical stress, from the GREMAN Laboratory, François-Rabelais University, Tours, France, in 2012.

In 2012, he became an Assistant Professor with the IUT of Cachan, Université Paris-Saclay, Gif-sur-Yvette, France, and joined the Group of Electrical Engineering of Paris (GeePs), Paris, France. His main research interests include the characterization of electromagnetomechanical couplings, the definition of constitutive laws by phenomenological approaches, and the prediction of such coupled phenomena by considering multiscale methods.

Anastasios Skarlatos (Member, IEEE) received the Diploma degree in electrical engineering from the University of Patras, Patras, Greece, in 1998, and the Ph.D. degree from the Technische Universität Darmstadt, Darmstadt, Germany, in 2003.

He currently occupies the position of Senior Researcher at CEA, LIST, Université Paris-Saclay, Gif-sur-Yvette, France. His main research interests include the development of semianalytical, numerical and hybrid methods for the treatment of near-field scattering problems in electromagnetism and heat propagation with applications in nondestructive testing. He is also active in the area of material evaluation via magnetic methods with the development of numerical tools for the treatment of the hysteresis problem, postprocessing, and data inversion.

Laurent Daniel received the Ph.D. degree from the Ecole Normale Supérieure de Cachan, Cachan, France, in 2003, and the Habilitation degree in physics from the Université Paris-Sud, Orsay, France, in 2011.

Since 2015, he has been a Full Professor with the CentraleSupélec, Université Paris-Saclay, Gif sur Yvette, France. His research activities, within the Group of Electrical Engineering of Paris (GeePs), Paris, France, are dedicated to electromechanical and magnetomechanical couplings in materials for electrical engineering applications. He is notably involved in the definition of multiscale methods for the prediction of such coupled phenomena and in the development of dedicated experimental characterization setups. Since 2014, he has been the Director of the Automotive Mechatronics Chair, a partnership between CentraleSupélec, Gif-sur-Yvette; Esigelec, Saint-Etienne du Rouvray, France; and the automotive company Forvia, Nanterre, France.

Christophe Reboud received the degree in engineering and the master's degree from the Ecole Centrale de Nantes, in 2003, and the Ph.D. degree in signal processing from the University Paris Sud XI, Orsay, France, in 2006.

He was with CEA, LIST, Gif-sur-Yvette, France, where he was in charge of electromagnetic modeling for nondestructive testing (NDT) applications. He specialized in semianalytical methods for efficient simulation of eddy current testing problems, as well as metamodeling and statistical studies for reliability assessment. Since 2012, he has been with the NDT Department, CEA LIST, where he has been responsible for the electromagnetic modeling laboratory inside the. He is currently a Senior Expert of CEA in the fields of NDT techniques, electromagnetics, and modeling.